INSTITUTE OF PHYSICS PUBLISHING MEASUREMENT SCIENCE AND TECHNOLOGY

Meas. Sci. Technol. **17** (2006) 761–770 doi:10.1088/0957-0233/17/4/023

The characteristics of the particle position along an optical axis in particle holography

Y J Choo and B S Kang

Department of Mechanical Engineering, Chonnam National University, 300, Yongbong-Dong, Buk-Gu, Gwangju 500-757, Korea

Received 12 July 2005, in final form 24 January 2006
Published 21 February 2006
Online at stacks.iop.org/MST/17/761

Abstract

Particle diagnostics involving three-dimensional distributions are important topics in many engineering fields. The holographic particle velocimetry system is a promising optical tool for measuring three-dimensional particle velocities. One of the inherent limitations of particle holography is the very long depth of field of particle images, which causes considerable difficulty in the determination of particle positions along the optical axis. In this study, diffused illumination holography was adopted as a tool for analysing the characteristics of particles. The prerequisites for a more precise determination of the velocities of particles are a profound understanding of image properties and of the focusing parameter used to determine the particle position along an optical axis. For this purpose, the characteristics of speckles and particle images were investigated with respect to variations in hologram aperture and particle position along the optical axis. Based on our findings, we introduced three auto-focusing parameters corresponding to the sizes of particles, namely, correlation coefficient, sharpness index and depth intensity, to determine the focal plane of a particle along the optical axis. To investigate the suitability of these parameters, the plane image of a dot array screen containing different dot sizes was recorded and the positions of each dot along the optical axis were evaluated. In addition, the effect of particle distance from the holographic film was examined by changing the distance between the screen and the holographic film. All measurement results verified that the evaluated positions throughout the suggested auto-focusing parameters remain within acceptable error ranges. These research results may provide fundamental information for the development of a holographic velocimetry system based on automatic image processing.

Keywords: three-dimensional position of particles, holography, holographic velocimetry

1. Introduction

The flow fields encountered in many engineering areas have many complexities and irregularities, and a three-dimensional nature. To investigate the characteristics of such flow fields, various measurement techniques and instruments have been developed and commercialized. Among these, non-intrusive optical instruments, such as LDV (laser Doppler velocimetry) and PIV (particle image velocimetry) have advanced remarkably because of rapid laser, imaging system and computer developments. However, a measurement tool capable of measuring 3D velocities over a complete test volume as a function of time remains on the developmental wish list. In recent years, research on flow field measurement tools has concentrated on 3D velocity measurements. Even though the extension of 2D PIV to 3D, for example, a method of scanning light sheet or a stereoscopic method [1], seems to be reasonable from a short-term standpoint, a holographic

method probably offers the ultimate solution, because of its superiority at realizing 3D fields. However, many problems must be overcome, and holographic systems very much remain at the developmental level.

As for spray diagnostic systems, the considerable progress made in laser instrument technologies such as PDPA (phase Doppler particle analyser) now make it possible to obtain reliable data on droplet sizes and velocities in dilute sprays. However, these methods are inherently limited in dense spray regions, where liquid elements are rather large and non-spherical. In addition, no information on spray structure can be provided by this kind of instrument. On the other hand, the holographic technique reproduces the frozen spray as a 3D image, from which droplet sizes and 3D velocities and spray structures can be investigated.

The holographic technique has been widely used for some time by those researching particle sizing [2]. Interest in the use of holography as a tool for 3D particle velocity determination has increased recently with the aim of making full use of the 3D capabilities of holography. Holographic particle velocimetry systems reported to this date fall into two categories involving (1) direct measurements of particle sizes and displacements from images [3–6], and (2) holographic PIV, which extends the correlation technique used in 2D PIV to three dimensions [7–10]. The ultimate goal of the present research is to develop a system that can be placed in the first category.

One of the inherent characteristics of particle holography using plane or spherical waves as an object beam is the very deep depth of field of particle images compared with the comparative shallow depth of field of a normal optical camera. This characteristic causes considerable difficulty during the determination of particle positions on the optical axis, and prevents full automation of holographic image processing from image capture to particle characterization in space and time.

In this study, diffused illumination holography was adopted to avoid the problem of the long depth of field in the analysis of particle characteristics. The prerequisites required to precisely determine particle velocities are profound understanding of the image properties and focusing parameters used to determine the particle position along an optical axis. To facilitate this, we investigated the characteristics of speckles and particle images versus hologram aperture and particle positions along the optical axis. Accordingly, we introduced three auto-focusing parameters corresponding to the sizes of particles, namely, correlation coefficient, sharpness index and depth intensity to determine the focal plane occupied by particles along the optical axis. To confirm the suitabilities of the above parameters, a plane image of a dot array screen containing different dot sizes was recorded and the positions of each dot on the optical axis were evaluated. In addition, the effect of the particle distance from the holographic film was examined by changing the distance between the screen and the holographic film. It was confirmed in the preliminary experiments of the next stage of this research that the application of the developed methods in the present study to real spray droplets created no difficulties.

2. Hologram recording and reconstruction

The holographic recording system, which is not shown here for brevity, is a typical off-axis holography. The light source

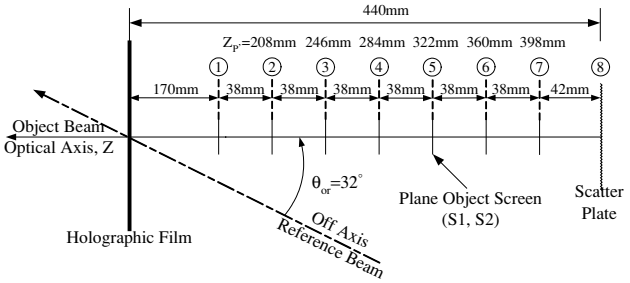

Figure 1. Recording conditions.

used to fabricate holograms was a diode pumped crystal laser (CrystaLaser Co.), which generated a wavelength of 532 nm, vertically polarized, and 500 mW CW output laser beams. The holographic plate used in our research was Slavich's VRP-M, which features the spectral sensitivity at 532 nm and resolving power of 3000 lines mm^{-1}. The recording conditions are shown in figure 1. Instead of recording real particles, two transparent screens of dark dots were used for convenience and to aid systematic investigation. Screen 1 (S1) contained various dot sizes (D_p) ranging from 8 to 300 μm, and screen 2 (S2) (48.5 × 48.5 mm^2) was a dot array which has equally spaced dots (500 μm size) in two directions, 33 dots in each direction (total 1089 dots). A diffuser was fixed at $z_S = 440$ mm from the holographic film to provide a uniform background and to decrease image depth of field. To investigate the effect of the particle position on the holographic film, the distance between each screen and the holographic film was changed from no. 1 ($z_p = 170$ mm) to no. 8 ($z_p = 440$ mm).

The coordinates of the recording and reconstruction systems with the centre of the hologram as origin are shown in figure 2. The object beam is directed along the Z axis and the X–Y plane lies normal to this axis. During recording, the diffuser and the screens are in the left space (the $-Z$ axis) of the holographic film. The coordinate of the centre of an arbitrary dot on the screens is $(-x_{p'}, y_{p'}, -z_{p'})$. To investigate the effect of the hologram aperture, the diameter of a diaphragm, D_H, positioned in front of a hologram was altered; $D_H = 10$, 20, 30, 50, 70 and 100 mm.

The recorded holograms were developed, fixed and dried as for photographic film processing, and then reconstructed and analysed using an image processing system. To avoid image aberrations, the optical system used for recording was also used for the reconstruction process, including the laser. Instead of reconstructing virtual images, real particle images were reconstructed in the right space (the $+Z$ axis) of the hologram using the conjugate reference beam obtained by rotating the hologram by 180° with respect to the Y axis. No lens was used for the digital CCD camera (Kodak Co., MegaPlus ES 1.0, 1024 × 1024 pixels, 9 μm pixel size) to exclude extension of the depth of field by a lens, and to obtain as wide an angular aperture as possible. The camera was moved automatically using a three-axis translation stage (PI Inc.) and positioned with a resolution of 33 nm.

The plane where the camera sensor is located is defined as the image plane and the coordinate of a pixel in the sensor is (x_I, y_I, z_I). The image of one particle with its speckle background is defined as a region of interest (ROI). Supposing

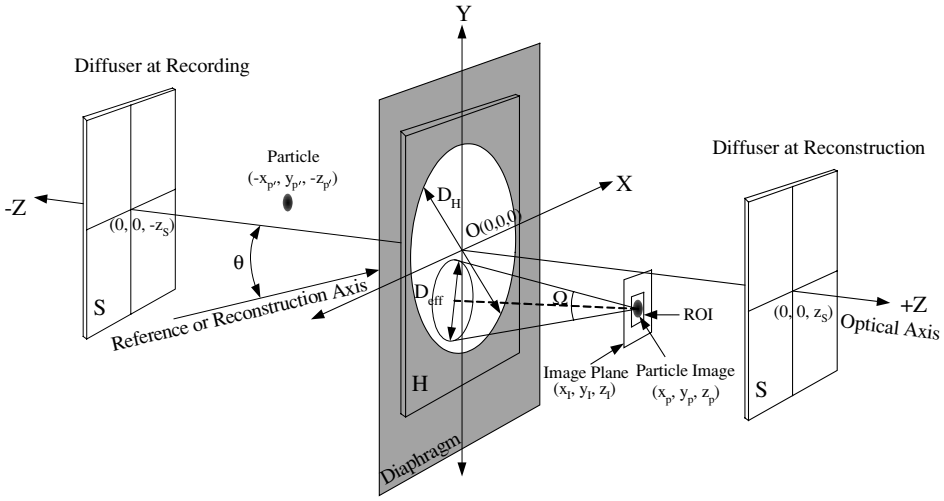

Figure 2. Coordinates of the recording and reconstruction systems.

a hologram is reconstructed with a magnification of 1, without aberrations, the reconstructed coordinate of a focused particle, (x_p, y_p, z_p), should be equal to $(x_{p'}, y_{p'}, z_{p'})$. The diameter of the hologram, which contributes to the formation of a particle in a ROI, is defined as the effective diameter, D_{eff}, and the angular aperture, Ω, is defined as the solid angle subtended by the circle of diameter D_{eff} from the focused particle. The diffuser is reconstructed at $z = z_s$ from the hologram.

Reconstructed images can be analysed by the sequential-process during the reconstruction or by the post-process after acquiring all images. In this study, the latter method was used to avoid the long instrument operation times required for real-time analysis. Thus, all reconstructed images were first captured using the camera moved by the same distance along the optical axis. To do this, an adequate interval of camera movement should be predetermined because the minimum resolution of image analysis along the optical axis (the Z axis) is determined by the pre-set interval and the effectiveness of image analysis depends on the interval of camera movement. Considering the depth of field of the smallest particle, the interval of camera movement was set at 33 μm which was 1000 times the minimum resolution of the translation stage.

3. Characteristics of the reconstructed images

3.1. Speckle background

Diffused illumination holography has some advantages such as reduced depth of focus, uniform background and minimized noise compared with conventional particle holography using plane waves. Simultaneously, the speckle noise, which is unavoidable due to the diffused object beam, prevents the recognition of particle image against speckle background. Moreover, the properties of these speckles are changed by recording conditions such as angular aperture, properties of the object beam source and the position of the observation plane. Therefore, it is necessary to understand the characteristics of speckles in order to achieve more precise determination of particle positions along the optical axis. In this research, we compared experimentally measured properties of speckles with theoretically predicted ones and investigated how the properties of speckles affect the image quality and position estimation of the reconstructed particles.

Speckles are commonly described in terms of their statistically determined intensities and sizes [11–13]. The probability density function (PDF), $P(I)$, of speckle intensity is expressed as

$$P_I(I) = (B/\bar{I})^B I^{B-1} \frac{\exp[-B(I/\bar{I})]}{\Gamma(B)} \tag{1}$$

$$B = (\bar{I})^2/\sigma_I^2, \qquad \sigma_I^2 = (\overline{I^2}) - (\bar{I})^2 \tag{2}$$

$$C = \frac{\sigma_I}{\bar{I}} = \frac{1}{B^{0.5}}, \tag{3}$$

where I is the intensity at a point, $\bar{I}$ is the intensity averaged over the transverse plane, σ is the standard deviation, Γ is the gamma function, B is the shape constant (always larger than 1) and C is the contrast (always smaller than 1). As B and C approach 1, object recognition capability decreases.

Speckles can be described as micro or macro based on whether the speckle size is smaller or larger than the pixel size. Although both speckle types detrimentally affect image analysis, macro speckles present more of a problem for the analysis of small particles, as in the present study [14, 15]. Measured probability density distributions are compared with the theoretical PDF using equation (1) in figure 3. Inserted photographs show typical micro (figure 3(*a*)) and macro speckle patterns (figure 3(*b*)). Micro speckles have uniform background so it is relatively easy to recognize particle images from background. For macro speckles, on the other hand, it is difficult to separate particles from background due to high contrast of intensities. Particularly, it could be much worse for smaller size of particles than the speckle size. For the PDF of speckle intensity, macro speckles generally show disagreement with the theoretical PDF based on previous research. In the present case, micro speckles start to appear when the value of B is larger than 2.5 ($C = 0.16$). For macro speckles, it is close to 1 and the theoretical PDF deviates from the measured probability density distribution. Figure 4 shows the effects of hologram aperture, D_{H}, and imaging plane location, z_I, along the optical axis on the shape constant and the contrast. As the hologram aperture decreases and when the imaging plane

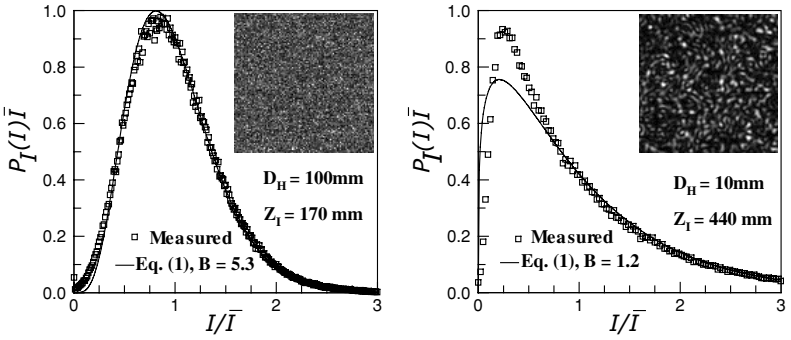

Figure 3. Typical speckle pattern and probability density function; (*a*) micro speckle, $D_{\mathrm{H}} = 100$ mm, $z_I = 170$ mm, $B = 5.3$ and (*b*) macro speckle, $D_{\mathrm{H}} = 10$ mm, $z_I = 440$ mm, $B = 1.2$.

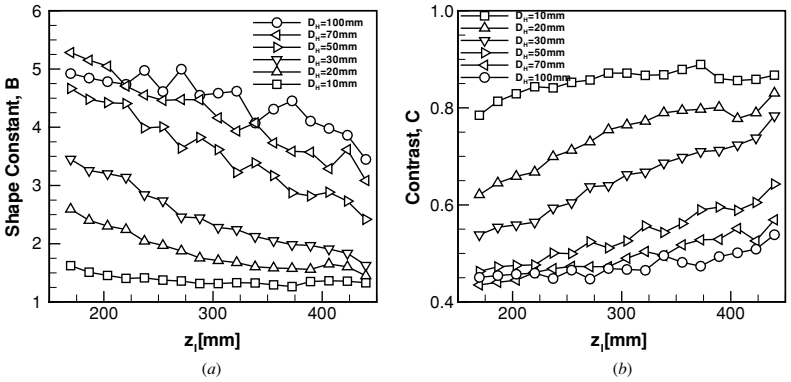

(*a*) (*b*)

Figure 4. (*a*) Shape constant and (*b*) speckle contrast variations along the *Z* axis at different hologram apertures, D_{H}.

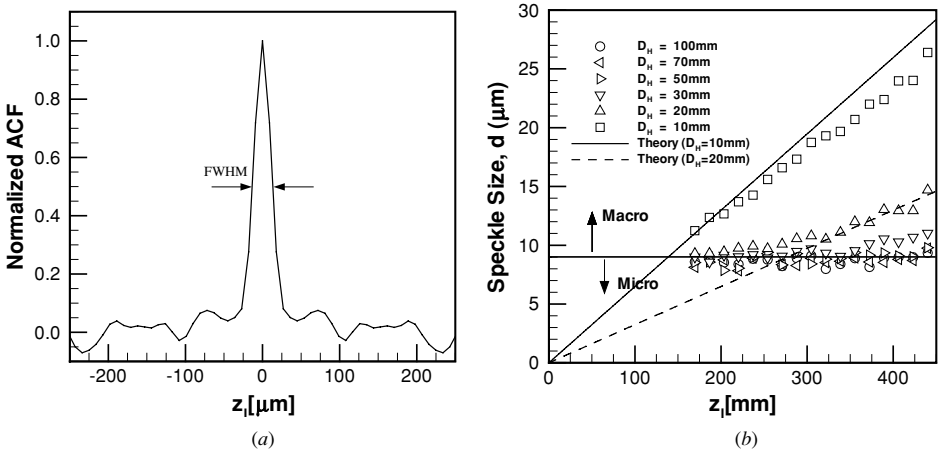

(*a*) (*b*)

Figure 5. Characteristics of speckle size; (*a*) normalized auto-covariance function and (*b*) speckle size along the *Z* axis at different hologram apertures, D_{H}.

is moved further from the hologram, B and C approach 1, which means that particle image quality deteriorates due to the presence of speckles.

The second characteristic of speckles is size, d. Generally, the size of speckle produced by illuminating a diffusing surface with a high coherent laser can be theoretically predicted as

$$d = 1.22\lambda z_I / L, \tag{4}$$

where λ is the laser wavelength, z_I is the distance between the diffusing surface and the observation plane and L is the characteristic length of the diffusing surface. In our case, z_I is the distance between the hologram and the imaging plane and L is equal to the effective diameter of the hologram, D_{eff}.

The other method of experimentally obtaining the speckle size is to use the auto-covariance function (ACF) [15]. If ΔI is the discrete image function that describes speckles, the discrete ACF can be expressed as

$$\mathrm{ACF}(m,n) = \sum_{k=1}^{M}\sum_{l=1}^{N} \Delta I(k,l)\Delta I[(k+m),(l+n)],$$
$$\Delta I(m,n) = I(m,n) - \bar{I}, \tag{5}$$

where m and n are pixel indices, and M and N are the image dimensions in pixels. Instead of using 2D ACF defined in equation (5), the sum of all 1D ACF in one direction was calculated and normalized by its maximum. Figure 5(*a*)

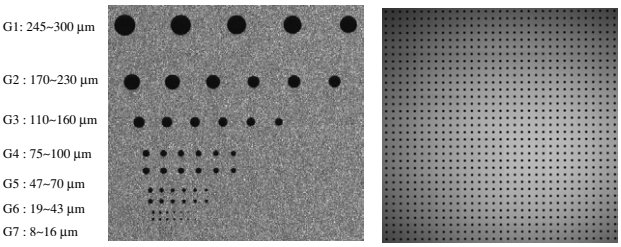

Figure 6. Typical reconstructed image of screens at $z_p = 170$ mm; (*a*) screen S1; the largest particle size is 300 μm and (*b*) screen S2; dot size is 500 μm and the pitch of each dot is 1.5 mm.

shows the normalized ACF for the speckle pattern shown in figure 3(*b*). Here, full width half maximum (FWHM) can be considered as the speckle size. The effects of hologram aperture, D_{H}, and the location of the imaging plane along the optical axis, z_I, on the speckle size are shown in figure 5(*b*). The solid and dotted lines are the speckle size predicted by equation (4) for $D_{\mathrm{H}} = 10$ and 20 mm, respectively. Except for the $D_{\mathrm{H}} = 10$ and 20 mm cases, the approximate maximum size of speckle predicted experimentally is below the camera pixel size, i.e., 9 μm. Thus, the size of a macro speckle larger than a pixel can be obtained using the above method. On the other hand, it is difficult to obtain the size of micro speckles using the ACF and the predicted sizes of speckles are almost equal to the size of one CCD camera pixel [15]. Based on the above observations, the hologram aperture should be maximized and particles should be positioned close to the hologram to reduce the effect of speckles. The hologram aperture was set at D_{H} =100 mm in subsequent experiments, which is the same diameter as the object beam used for recording.

3.2. Particle images

Figure 6 shows the reconstructed image of screens S1 (figure 6(*a*)) and S2 (figure 6(*b*)) at z_p =170 mm. Careful inspection of reconstructed screen images showed that reconstructed images showed consistent magnifications and aberrations that can be predicted theoretically. From the image of screen S1, the smallest particle size by naked-eye observation was about 20 μm. Below this size, only one or two pixels corresponded to a particle, and they were too small to analyse in view of the degradation of quality by speckles and the capabilities of holographic reconstruction. Images of screen S2 showed that distances between centres of dots exactly matched real distances, thus demonstrating the accuracy of the reconstructed transverse particle position. The focused images of a 300 μm dot are shown in figure 7 at different particle positions along the optical axis. Even

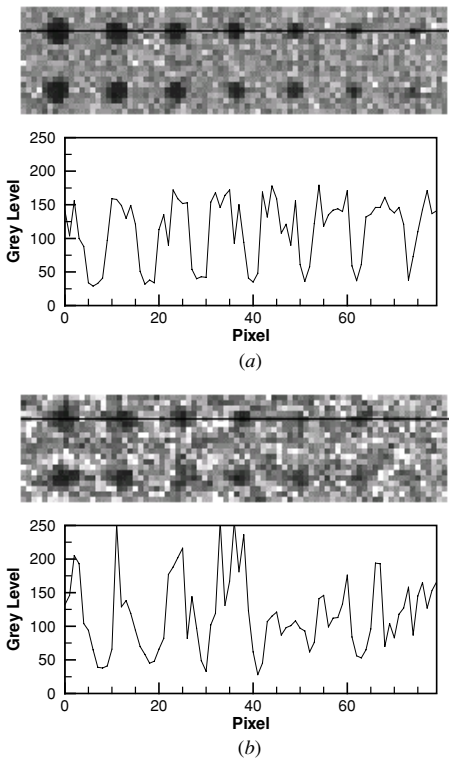

Figure 8. Particle image of G6 group on screen S1 and line profile of intensity; (*a*) $z_p = 170$ mm and (*b*) $z_p = 440$ mm.

though quantitative analysis could not be performed when this particle was moved further from the hologram, macro speckles appeared in images and caused a gradual degradation in image quality, especially at the boundary of the particle. Figure 8 shows the image and the horizontal centre profile of grey level of particles in G6 group at $z_p = 170$ mm (figure 8(*a*)) and 440 mm (figure 8(*b*)). It reconfirms that the pattern of grey level demonstrating the existence of particles becomes very irregular as a particle is moved further from the hologram.

In addition to the effect of speckles, one more reason for the degradation of image quality as particle/hologram distance increases is the aberration shown in figure 9. The reconstructed wave front from three points (h_1, h_2, h_3) on the hologram should converge to a point light source on the reconstructed diffuser surface if aberration can be neglected [16]. In a real situation, however, the wave fronts from three points (h_1, h_2, h_3) are deviated to different points $(h_{1'}, h_{2'}, h_{3'})$ resulting in aberrations δ_1, δ_2, δ_3, respectively. Aberrations may result for various reasons such as different wavelengths of laser, misalignment of optical components, deformation during the chemical process of holograms and usage of lenses

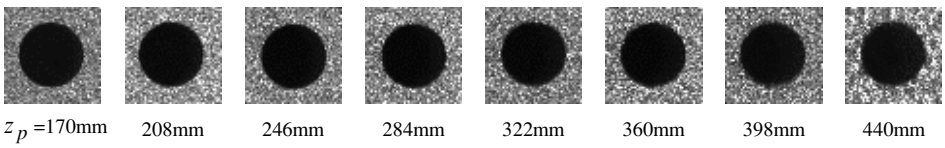

Figure 7. Sharpness of a 300 μm dot on S1 screen at each z_p.

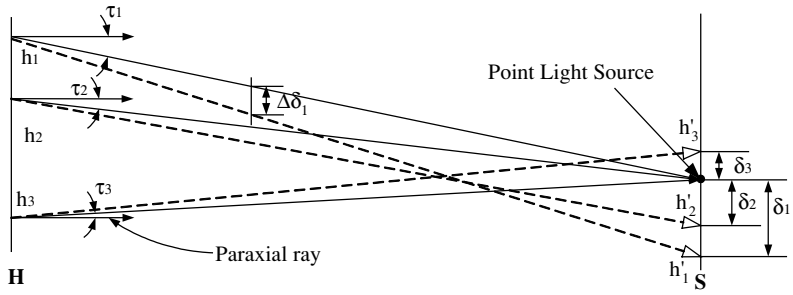

Figure 9. Image displacement originating from aberration.

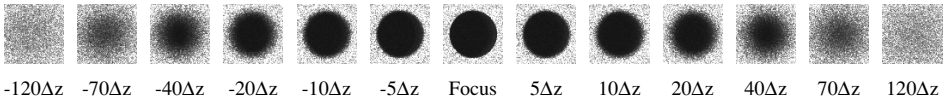

Figure 10. Defocusing pattern of a 500 μm dot at the centre of screen S2.

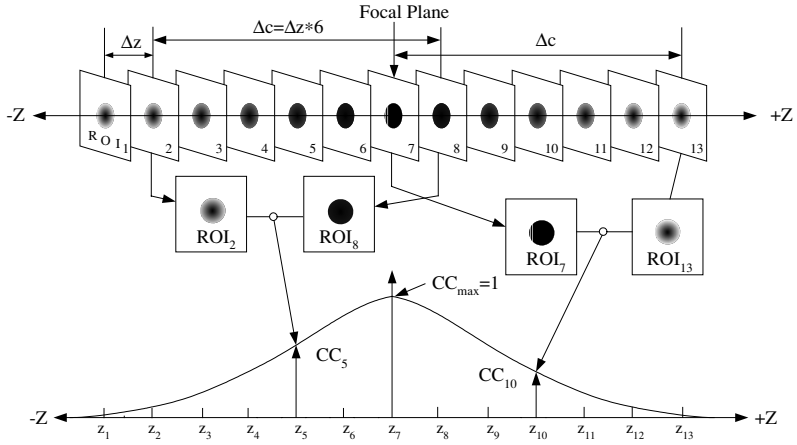

Figure 11. The correlation coefficient method using ROI-series images.

with spherical surfaces. This aberration depends on the angle τ formed between the ray from the point and a paraxial ray. The magnitude of this aberration reduces as the particle approaches the hologram. Therefore, when the particle/hologram distance is large, the degree of deviation due to aberration is large, as can be seen in figures 7 and 8.

4. Focusing parameters

In particle holography, the exact coordinates of particles at two moments in time should first be determined to evaluate particle velocities. The X and Y coordinates can be determined easily but the determination of the Z coordinate is not straightforward due to the large depth of field of the reconstructed particle images. The gradual defocusing pattern of a 500 μm dot at the centre of screen S2 by moving the camera along the optical axis is shown in figure 10. To determine the exact focal plane of a particle along the optical axis regardless of depth of field, appropriate auto-focusing parameters are required. Several criteria such as particle patterns, grey level distributions or grey level gradients can be used in photographically captured images. However, those criteria cannot be used for the holographically reconstructed images due to the presence of speckles. In this study, three new auto-focusing parameters corresponding to the particle size are proposed, namely, (1) correlation coefficient, (2) sharpness index and (3) depth intensity.

4.1. The correlation coefficient method (CCM)

The correlation coefficient, CC, between images represents how similar two images are or how closely two images are related, and is defined as

$$\mathrm{CC} = \frac{\sum_m \sum_n (F_{mn} - \bar{F})(G_{mn} - \bar{G})}{\sqrt{\left(\sum_m \sum_n (F_{mn} - \bar{F})^2\right)\left(\sum_m \sum_n (G_{mn} - \bar{G})^2\right)}}, \quad (6)$$

where m and n are pixel indices, F and G are images, $\bar{F}$ and $\bar{G}$ are the average grey values of each image. The value of CC approaches 0 if similarity between images is low and 1 if they are similar.

Figure 11 shows schematically how to determine the axial positions of particles using correlation coefficients. The correlation coefficient of a particle on an arbitrary plane in the optical axis is evaluated using two images at the same distance, namely, as the interval of correlation, ΔC_z, from that plane. The appropriate interval of correlation

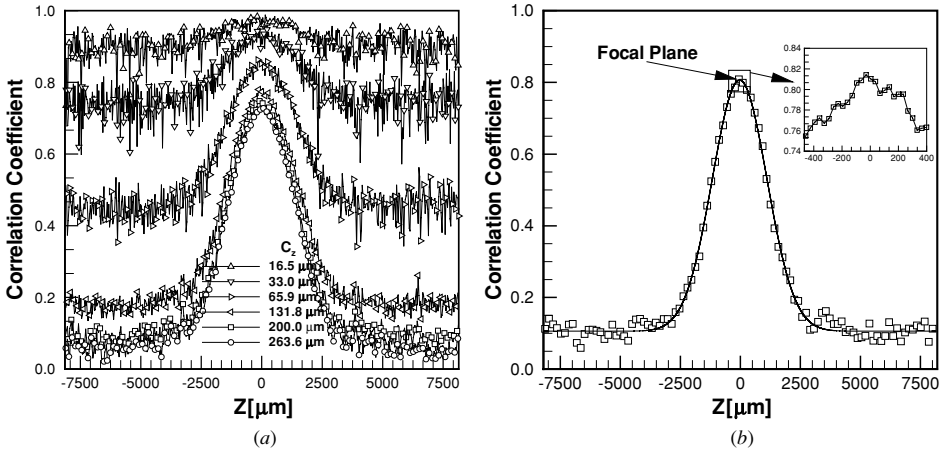

Figure 12. Correlation coefficient; (*a*) effect of correlation interval, ΔC_z, with $z_p = 322$ mm, $D_p = 300$ μm and (*b*) Gaussian curve fitting with $z_p = 170$ mm, $D_p = 300$ μm, $\Delta C_z = 200$ μm.

should be determined in advance to include the correlation effect of particles only, i.e., without any correlation effect of background. Figure 12(*a*) shows the distribution of correlation coefficients for a 300 μm particle on screen S1 by changing the interval of correlation. As the interval of correlation is reduced, the correlation coefficient increases, but the difference between maximum and minimum values is small, because the correlation effects of speckles and particles are high at small interval of correlation. As the interval of correlation increases, the difference becomes large because the correlation effect of particles with a large depth of field becomes greater than that of speckles, which provides a better distribution of correlation coefficients for the determination of the focal plane. Too high a correlation interval decreases the magnitude of the correlation coefficient and the difference between maximum and minimum values, because the correlation effects of speckles and of particles become small. Based on this, the determined optimum value of the interval of correlation was $\Delta C_z = 200$ μm.

The correlation coefficient shown in figure 12(*b*) can be approximated using the Gaussian curve fitting, and the centre of the curve fitting can be taken to represent the focal plane of a particle. Figure 13 shows the correlation coefficient distribution with changing particle size. As a particle becomes smaller, the distribution becomes highly irregular, which means that the correlation coefficient cannot be used any more due to a diminutive particle size. This is why the third parameter, depth intensity, was introduced for small particles.

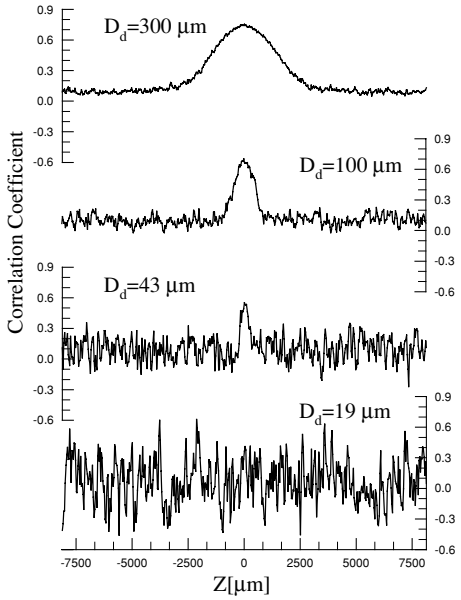

Figure 13. Correlation coefficient distributions on changing particle sizes on screen S1 ($D_p = 19, 43, 100, 300$ μm).

4.2. The sharpness index method (SIM)

The sharpness index is a measure of particle boundary sharpness. Figure 14 shows the typical pattern of a grey value histogram of a dot image. Three distinctive regions can be observed in the histogram. The left region of the histograms indicates the foreground, i.e., particles, and the right region the background. The region representing the particle boundary lies between these two regions, and their low values indicate a well-focused image with sharp boundary of particle. However, boundary sharpness can be expressed better using a cumulative histogram rather than simple histograms. The cumulative histogram is shown as a dotted line in figure 14, and shows a linear region connecting the region for background and that for particles. The slope of this linear region represents boundary sharpness, i.e., a lower slope indicates a sharper boundary. Therefore, this slope can be used as a focusing parameter, namely, which we refer to as the sharpness index.

A typical sharpness index for a 500 μm particle on screen S2 is shown in figure 15. As expected, the sharpness index shows a minimum and the axial coordinate at this minimum value can be considered to represent the particle focal plane. As compared with the correlation coefficient method, the axial width required to determine the focal plane is relatively small.

4.3. The depth intensity method (DIM)

For very small particles ($D < 50$ μm), the above two methods are not easily applied. A new focusing parameter for small

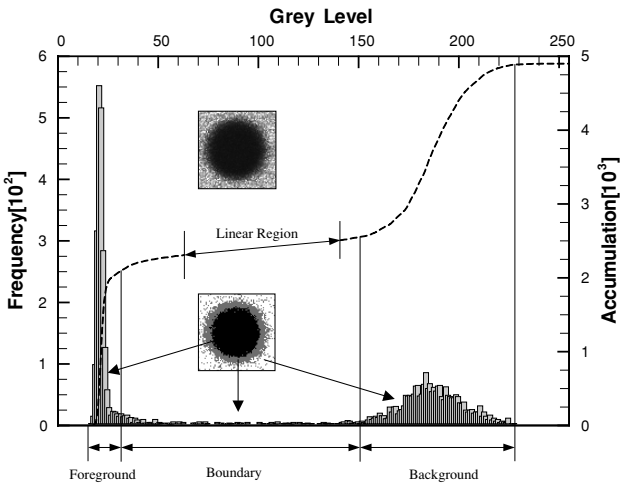

Figure 14. Illustration of the sharpness index method.

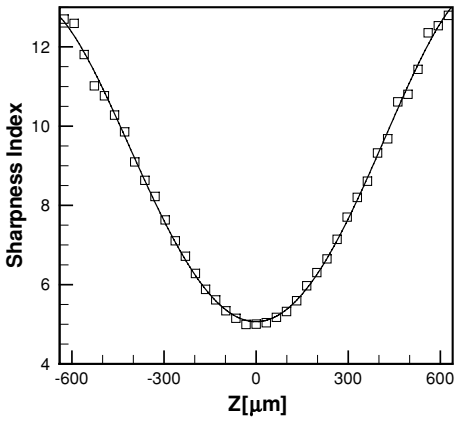

Figure 15. Sharpness index around the focal position with $D_p = 500\ \mu$m.

particles, namely, depth intensity, is introduced. Figure 16 schematically shows the depth intensity method to determine the focal plane of a small particle. Figure 16(*a*) represents the region of interest ($M \times N$) in the X–Y plane, ROI_{xy}, and the ROI_{xy}-series are obtained with an interval of Δz for the region of space in which the particle exists as shown in figure 16(*b*). If we cut the images of the ROI_{xy}-series using the X–Z or Y–Z slicing planes, as shown in figure 16(*b*), the region of interest ($M \times K$ or $N \times K$) in the Z axis, ROI_z, is obtained. The final image of ROI_z shown in figure 16(*c*) is the result of filtering using a smoothing operator and enhancing the contrast to improve position determination.

If the grey value of the cross-section images is plotted along the optical axis, we can obtain the depth intensity distribution, which again has the lowest value at the focal plane of a particle, because the grey value of a particle centre increases as the distance from the focal plane increases. The $M/2$nd row vector of the ROI_z image is the depth intensity distribution. These distributions for particles lower than 50 μm are shown in figure 17. All particles showed minimum values at the focal plane, thus indicating that this method can be used for small particles.

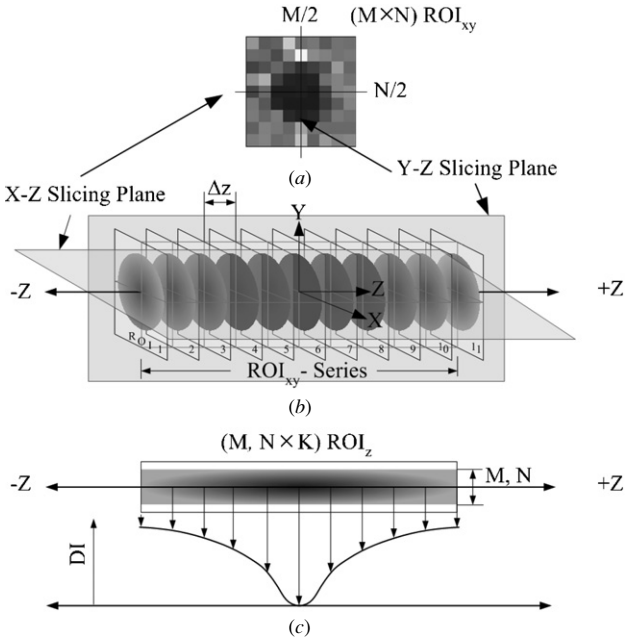

Figure 16. Illustration of the depth intensity method; (*a*) ROI_{xy} image, (*b*) slicing planes for ROI_z and (*c*) depth intensity of ROI_z.

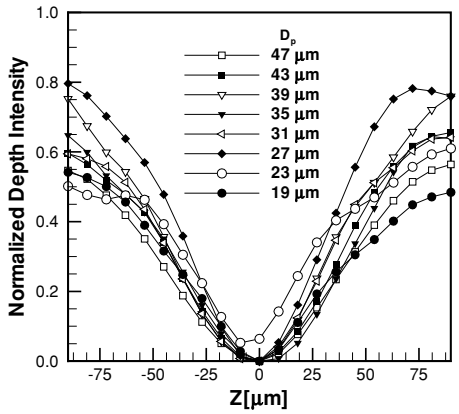

Figure 17. Depth intensity of small particles <50 μm.

4.4. Size dependence

The three focusing parameters introduced above respond differently to particle size. The correlation coefficient method can be applied except for small particles (<50 μm). However, as the size of a particle increases, the correlation coefficient distribution in the vicinity of the focal plane shows noticeable errors. Therefore, the focal plane should be determined using the Gaussian distribution of correlation coefficients obtained from the entire region occupied by a particle. Compared with the correlation coefficient method, the images with relatively small width along the optical axis are enough for the sharpness index method. High accuracies at determining the focal plane are expected for the cases of high number of particle pixels or high resolution of particle images. The depth intensity method relies on the grey value of the centre of a particle and thus it is not effective for large particles because the variation of this grey value diminishes with increasing particle size. On the other hand, the method is highly effective for small particles having small depth of field.

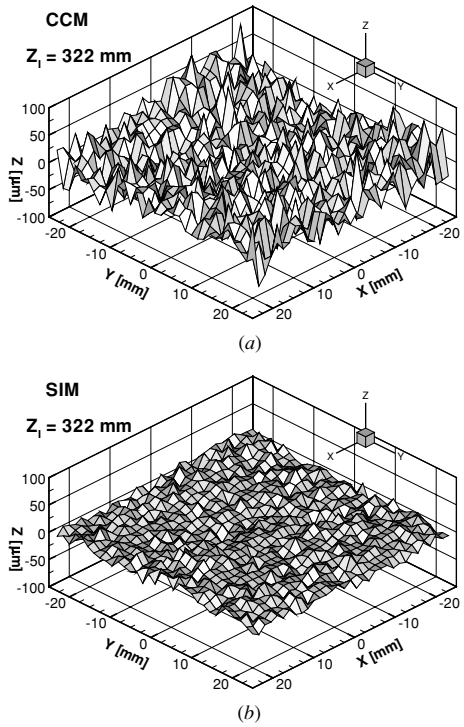

Figure 18. Reconstructed position of particles on screen S2 at $z_p =$ 322 mm; (*a*) CCM and (*b*) SIM.

In terms of the above characteristics, appropriate focusing parameters corresponding to the particle sizes were determined and applied as shown below.

- Large size particles ($D > 300$ μm): CCM and then SIM
- Medium size particles (50 μm $< D < 300$ μm): CCM
- Small size particles ($D < 50$ μm): DIM

5. Determination of axial position of particles

Reconstructed axial positions of particles on screen S2 at $z_p = 322$ mm were calculated by CCM or SIM as shown in figure 18. Ideally, particles should have the same reconstructed axial position because they exist in one plane, but the predicted axial positions of particles show some deviation from the plane of the screen. The total error, E, is defined as the difference between the predicted and real positions of a particle, and it is expressed as

$$E = z_p - z_{p'} = \bar{z}_p \pm u_z = \bar{z}_p \pm t_{v,p} S_z = E_{\text{bias}} \pm E_{\text{pre}}, \quad (7)$$

where $t_{v,p}$ is the t estimator for finite data sets, which is a function of the probability, $P(\%)$, and the degree of freedom, $v = N - 1$, and S_z is the standard deviation. The mean value of the total error can be considered as the bias error, E_{bias}, and the uncertainty as the precision error, E_{pre}. The bias error is a type of hardware error that occurs during the image recording and reconstruction processes and the precision error is a type of software error that occurs during the calculation process.

In figure 18, the mean value of the predicted positions of particles is zero and accordingly the bias error is also zero, which means that the plane obtained from predicted positions of particles is equal to the original position of the screen. The uncertainty of the CCM is $u_z = \pm 44.74$ μm and that of the SIM is $u_z = \pm 16.07$ μm (about 1/3 of CCM). Therefore, the SIM produces a better prediction of axial position than the CCM even though both methods can be applied to relatively large particles.

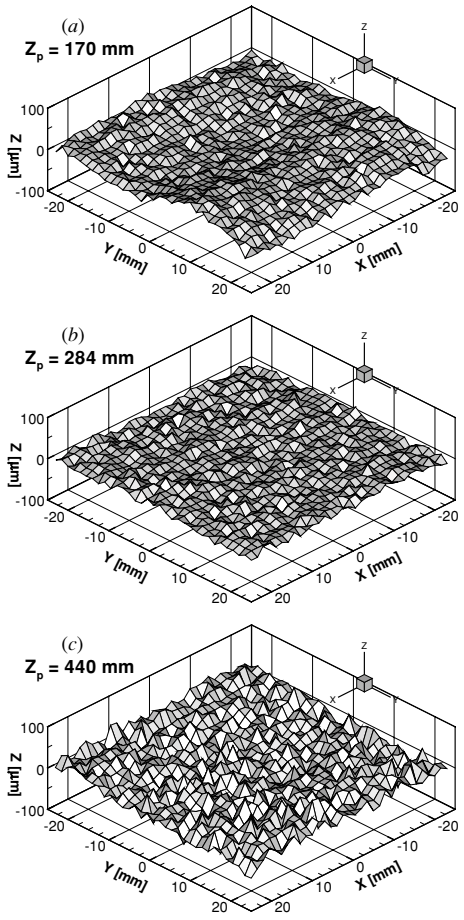

Figure 19. Reconstructed position of particles by CCM + SIM.

More accurate prediction of axial positions for relatively large particles is possible by the successive application of the CCM and the SIM. Specifically, the approximate focal plane of a particle is determined first by applying the CCM and then the SIM is used to determine the focal plane accurately using the reduced width of particle images around the pre-determined focal plane. The results of the successive applications of the CCM and the SIM to particle images on the screen S2 are shown in figure 19. In the case of the nearest screen position to the holographic film ($z_p = 170$ mm), the predicted positions of particles seem to be curved but the precision error representing deviation from the screen seems to be low. When a particle exists near the holographic film, the aperture of the hologram becomes narrow such that the whole region of the hologram cannot be reconstructed uniformly, which results in noticeable non-uniformity from place to place. However, the contrast of reconstructed particle images is fairly good due to relatively low aberration resulting in small precision errors. On the other hand, in the case of the farthest screen position from the holographic film ($z_p = 440$ mm), the bias error is not high owing to uniform reconstruction due to the wide hologram aperture. However, the precision error becomes large because the contrast of particle boundary is degraded by increased aberration.

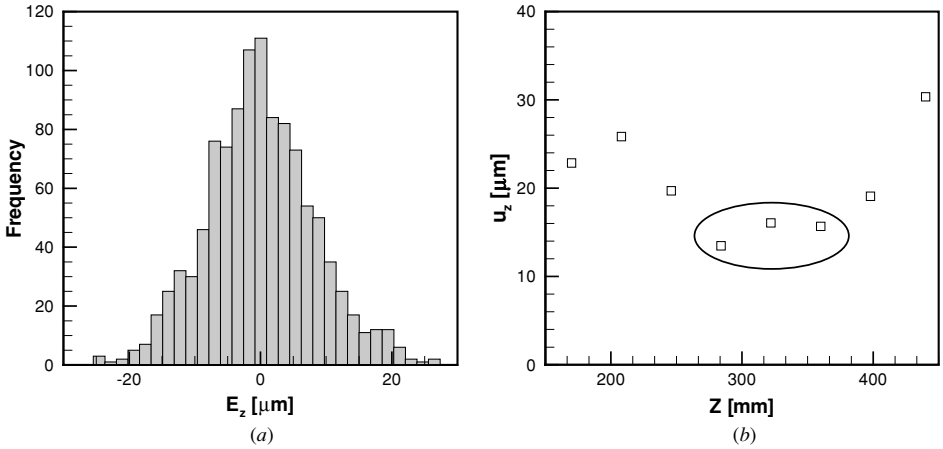

Figure 20. Position errors of particles reconstructed by CCM + SIM; (*a*) error histogram at $z_p = 322$ mm and (*b*) uncertainties of position errors along the Z axis.

Quantitative estimations of the total error are shown in figure 20. Figure 20(*a*) shows a typical histogram of total errors at $z_p = 322$ mm, and figure 20(*b*) shows the uncertainties of errors according to the holographic film/particle distance. Regardless of particle positions, the maximum and minimum values of uncertainties are ± 30 and ± 13 μm, respectively, which are relatively small errors considering a few millimetre order of depth of field of a particle. As particles approach or recede from the holographic film, the total error becomes high. For a particle close to the film, the error is mainly due to the optical system, which can be considered as a type of hardware error. On the other hand, for a distant particle, the error is mainly due to the procedure to determine the focal plane, a type of software error. Therefore, there exists an optimum particle position from the holographic film where the effect of these errors is minimized.

6. Conclusions

In this study, diffused illumination holography was adopted as a tool for analysing particle characteristics. Initially, the characteristics of speckles and particle images were investigated with respect to the hologram aperture and the particle position along the optical axis. Based on the results obtained, we introduced three auto-focusing parameters that depend on particle size, i.e., the correlation coefficient, sharpness index and depth intensity, to determine the focal plane of a particle along the optical axis. To investigate the suitability of the above parameters, the plane image of a dot array screen containing differently sized dots was recorded and the positions of dots on the optical axis were evaluated. In addition, the effect of particle location from the holographic film was examined by changing the holographic film/dot array screen distance. Our results show that particle positions determined using the suggested auto-focusing parameters remained within acceptable error limits. We hope that these research results provide useful information to those interested in developing a holographic velocimetry system based on automatic image processing.

Acknowledgment

This work was supported by the Korean Science and Engineering Foundation (grant no. R05-2000-000-00297-0).

References

[1] Hinsch K D 1995 Three-dimensional particle velocimetry *Meas. Sci. Technol.* **6** 742–53
[2] Vikram C S 1979 *Particle Field Holography* (New York: Cambridge University Press)
[3] Haussmann G and Lauterborn W 1980 Determination of size and position of fast moving gas bubbles in liquids by digital 3-D image processing of hologram reconstructions *Appl. Opt.* **19** 3529–35
[4] Kang B S 1995 A holographic study of the dense region of a spray created by two impinging jets *PhD Thesis* University of Illinois at Chicago, USA
[5] Feldmann O 1999 Short-time holography and holographic PIV applied to engineering problems *Applied Optical Measurements* (Berlin: Springer)
[6] Tao B, Malkiel E and Katz J 1999 *3rd Int. Workshop on Particle Image Velocimetry* pp 16–8
[7] Zimin V, Meng H and Hussain F 1993 Innovative holographic particle velocimeter; a multibeam technique *Opt. Lett.* **18** 1101–3
[8] Barnhart D H and Adrian R J 1994 Phase-conjugate holographic system for high-resolution particle-image velocimetry *Appl. Opt.* **33** 7159–70
[9] Meng H and Hussain F 1995 In-line recording and off-axis viewing technique for holographic particle velocimetry *Appl. Opt.* **34** 1827–40
[10] Zhang J, Tao B and Katz J 1997 Turbulent flow measurement in a square duct with hybrid holographic PIV *Exp. Fluids* **23** 373–81
[11] Goodman J W 1985 *Statistical Optics* (New York: Wiley)
[12] Jones R and Wykes C 1989 *Holographic and Speckle Interferometry* (Cambridge: Cambridge University Press)
[13] Alexander T L, Harvey J E and Weeks A R 1994 Average speckle size as a function of intensity threshold level: comparison of experimental measurements with theory *Appl. Opt.* **33** 8240–50
[14] Dallas W J 1978 Deterministic diffusers for holography *Appl. Opt.* **12** 1179–87
[15] Diamond F I 1969 Some effects of diffused illumination in holography *J. Opt. Soc. Am.* **59** 1339–42
[16] Champagne E B 1967 Nonparaxial imaging, magnification, and aberration properties in holography *J. Opt. Soc. Am.* **57** 51–5